SUPERCONDUCTIVITY

Discovery of a Cooper-pair density wave state in a transition-metal dichalcogenide

Xiaolong Liu[1]†, Yi Xue Chong[1]†, Rahul Sharma[1,2], J. C. Séamus Davis[1,3,4,5]*

Pair density wave (PDW) states are defined by a spatially modulating superconductive order parameter. To search for such states in transition-metal dichalcogenides (TMDs), we used high-speed atomic-resolution scanned Josephson-tunneling microscopy. We detected a PDW state whose electron-pair density and energy gap modulate spatially at the wave vectors of the preexisting charge density wave (CDW) state. The PDW couples linearly to both the *s*-wave superconductor and the CDW and exhibits commensurate domains with discommensuration phase slips at the boundaries, conforming those of the lattice-locked commensurate CDW. Nevertheless, we found a global $\delta\Phi \cong \pm 2\pi/3$ phase difference between the PDW and CDW states, possibly owing to the Cooper-pair wave function orbital content. Our findings presage pervasive PDW physics in the many other TMDs that sustain both CDW and superconducting states.

Transition-metal dichalcogenides (TMDs) are a rich platform for the exploration of quantum matter (*1*–*6*). In this context, a fundamental but elusive state is the electron-pair density wave (PDW) (*7*). Theoretically, the PDW state of TMDs was predicted to be generated by magnetic field (*8*), spin-valley locking (*9*), a CDW lock-in transition (*10*), and doping TMD bilayers (*11*); PDW melting into a charge-6*e* superfluid was also predicted (*12*). However, detecting the PDW state in a TMD experimentally has been challenging.

A familiar TMD state is the charge density wave (CDW): a charge density field $\rho_C(\boldsymbol{r})$ that modulates spatially at wave vectors $\boldsymbol{Q}_C^i (i = 1, 2, 3)$, which are not crystal reciprocal lattice vectors. Such a charge density modulation

$$\rho_C^i(\boldsymbol{r}) = \rho_i(\boldsymbol{r})e^{i\boldsymbol{Q}_C^i\cdot\boldsymbol{r}} + \rho_i^*(\boldsymbol{r})e^{-i\boldsymbol{Q}_C^i\cdot\boldsymbol{r}} \quad (1)$$

has a mean-field order parameter $\left\langle C_{\boldsymbol{k}}^\dagger C_{\boldsymbol{k}+\boldsymbol{Q}_C^i}\right\rangle$, where $C_{\boldsymbol{k}}^\dagger$ is the creation operator and $C_{\boldsymbol{k}}$ is the annihilation operator for single-electron $\boldsymbol{k}$-space eigenstates. The simplest TMD superconductor state is spatially homogeneous but breaks gauge symmetry

$$\Delta_S(\boldsymbol{r}) = \Delta_0 e^{i\phi} \quad (2)$$

with a mean-field order parameter $\left\langle C_{\boldsymbol{k}}^\dagger C_{-\boldsymbol{k}}^\dagger\right\rangle$. By contrast, a PDW state is described by an electron-pair field $\Delta_P(\boldsymbol{r})$ that modulates spatially at one or more wave vectors $\boldsymbol{Q}_P^i$

$$\Delta_P^i(\boldsymbol{r}) = \left[\Delta_i(\boldsymbol{r})e^{i\boldsymbol{Q}_P^i\cdot\boldsymbol{r}} + \Delta_i^*(\boldsymbol{r})e^{-i\boldsymbol{Q}_P^i\cdot\boldsymbol{r}}\right]e^{i\theta} \quad (3)$$

This state also breaks gauge symmetry, and its mean-field order parameter is $\left\langle C_{\boldsymbol{k}}^\dagger C_{-\boldsymbol{k}+\boldsymbol{Q}_P^i}^\dagger\right\rangle$. Sophisticated atomic-scale visualization of TMD states by using single-electron tunneling (*13*–*16*) has revealed CDW quantum phase transitions (*13*), a CDW Bragg glass (*14*), interfacial band alignment (*15*), and strain control of the CDW state (*16*). But to detect and image a PDW state in TMDs remained an experimental challenge.

Experimentally, the total electron-pair density $\rho_{CP}(\boldsymbol{r})$ might be visualized by measuring Josephson critical-current $I_J(\boldsymbol{r})$ to a superconducting scanning tunneling microscopy (STM) tip (*17*) because $\rho_{CP}(\boldsymbol{r}) \propto I_J^2(\boldsymbol{r})R_N^2(\boldsymbol{r})$, where R_N is the normal-state junction resistance (*18*, *19*). But this has proven impractical because the thermal fluctuation energy k_BT typically exceeds the Josephson energy $E_J = \Phi_0 I_J/2\pi$, where

$$I_J = \frac{\pi\Delta(T)}{2eR_N}\tanh\left[\frac{\Delta(T)}{2k_BT}\right] \quad (4)$$

(k_B, Boltzmann constant; T, temperature; $2e$, electron-pair charge; and Φ_0, magnetic flux quantum). Instead, when $E_J < k_BT$, the tip-sample Josephson junction exhibits a phase-diffusive (*20*–*22*) steady state at voltage V and electron-pair current

$$I_{CP}(V) = \frac{1}{2}I_J^2 ZV/\left(V^2 + V_c^2\right) \quad (5)$$

Here, $V_c = 2eZk_BT/\hbar$, where Z is the high-frequency impedance in series with the voltage source and $\hbar$ is Planck's constant h divided by 2π. From Eq. 5

$$dI_{CP}/dV \equiv g(V) = \frac{1}{2}I_J^2 Z\left(V_c^2 - V^2\right)/\left(V_c^2 + V^2\right)^2 \quad (6)$$

yields $g(0) \propto I_J^2$ (fig. S1) [(*23*), section 1]. Thus, spatially resolved measurements of $g(0, \boldsymbol{r})$ can provide a practical means (*24*–*28*) to image $I_J(\boldsymbol{r})$, so that the electron-pair density can then be visualized as $N_{CP}(\boldsymbol{r}) \equiv g(\boldsymbol{r}, 0)R_N^2(\boldsymbol{r}) \propto \rho_{CP}(\boldsymbol{r})$ [(*23*), section 1].

We studied bulk crystals of 2H-$NbSe_2$, a quasi–two-dimensional TMD with a robust CDW state (*29*). It has a hexagonal layered structure with Se-Se separation d and a Fermi surface with pockets surrounding the Γ and K points (fig. S2). The CDW phase transition at $T \approx 33.5$ K generates crystal and charge density modulations at three in-plane wave vectors $\boldsymbol{Q}_C^i \approx \{(1,0); (1/2, \sqrt{3}/2); (-1/2, \sqrt{3}/2)\}2\pi/3a_0$ ($a_0 = \sqrt{3}d/2$ is the unit cell dimension), and the s-wave superconductivity (SSC) transition at $T_C \approx 7.2$ K completely gaps the Fermi surface. We used atomic-resolution superconducting scan tips made of Nb (*17*) with a standard tip-energy-gap $|\Delta_T| \approx 0.9$ meV (fig. S3).

A typical topographic image $T(\boldsymbol{r}, V)$ of the Se-termination layer of $NbSe_2$ when using such tips is shown in Fig. 1A, with the CDW modulations appearing as $3a_0$ periodic intensity amplifications [Fig. 1A, inset, $T(\boldsymbol{q}, V)$] (*13*, *14*). A typical differential tunneling conductance spectrum $dI/dV|_V \equiv g(V)$ is shown in Fig. 1B. To simultaneously visualize the CDW, SSC, and any putative PDW states, a dynamic range exceeding 10^4 is required in the tip-sample voltage, spanning the CDW range from above ~50 mV (Fig. 1B), to the SSC energy gap range ~1 mV (Fig. 1C), to the Josephson pair-current range approaching ~10 μV (Fig. 1, D and E). Visualizing the quasiparticle densities $N_Q(\boldsymbol{r})$ of both CDW and SSC uses single-electron tunneling at energies indicated with the red and green arrows in Fig. 1, B and C, respectively. Visualizing electron-pair density $N_{CP}(\boldsymbol{r})$ of the condensate uses the phase-diffusive Josephson tunneling current $I_{CP}(V)$ or $g(0)$, indicated with the blue arrows in Fig. 1, D and E.

At T = 290 mK, we first imaged $N_Q(\boldsymbol{r}) \equiv g(\boldsymbol{r}, -20\text{ mV})$ at V = –20 mV, where CDW intensity is strong (*13*), with the results shown in Fig. 2A. Next, we imaged the normal-state resistance (fig. S4) of the tip-sample Josephson junction $R_N(\boldsymbol{r}) \equiv I^{-1}(\boldsymbol{r}, -45\text{ mV})$ (Fig. 2B). Third, we studied the electron-pair current by measuring $g(\boldsymbol{r}, 0)$ (Eq. 6) (Fig. 2C). All four independent images $T(\boldsymbol{r}, V)$: $N_Q(\boldsymbol{r})$: $R_N(\boldsymbol{r})$: $g(\boldsymbol{r}, 0)$ are registered to each other with precision of $\delta x \approx \delta y \lesssim 15$ pm (fig. S5) [(*23*), section 2]. This constitutes a typical data set for visualizing the crystal, CDW, SSC, and PDW states simultaneously; its acquisition required developing high-speed scanned Josephson-tunneling microscopy (SJTM) imaging protocols (fig. S6) [(*23*), section 3]. Eventually, to visualize the electron-pair density, we used the data in Fig. 2, B and C, to derive $N_{CP}(\boldsymbol{r}) \equiv g(\boldsymbol{r}, 0)R_N^2(\boldsymbol{r})$ (Fig. 2D). Here, we see electron-pair density modulations at three in-plane wave vectors $\boldsymbol{Q}_P^i \approx \{(1,0); (1/2, \sqrt{3}/2); (-1/2, \sqrt{3}/2)\}2\pi/$

[1]Laboratory of Atomic and Solid State Physics, Department of Physics, Cornell University, Ithaca, NY 14850, USA. [2]Department of Physics, University of Maryland, College Park, MD 20740, USA. [3]Department of Physics, University College Cork, Cork T12 R5C, Ireland. [4]Max Planck Institute for Chemical Physics of Solids, D-01187 Dresden, Germany. [5]Clarendon Laboratory, University of Oxford, Oxford OX1 3PU, UK.
*Corresponding author. Email: jcseamusdavis@gmail.com
†These authors contributed equally to this work.

$3a_0$, indicated with the blue circles in Fig. 2D, $N_{CP}(\boldsymbol{q})$ inset. Ultimately, in Fig. 2E, $N_C(\boldsymbol{r})$ of the CDW contains only the charge density modulations at $\boldsymbol{Q}_C^i$ (Fig. 2A), whereas in Fig. 2F, the simultaneous $N_P(\boldsymbol{r})$ of the PDW contains only the electron-pair density modulations at $\boldsymbol{Q}_P^i$ (Fig. 2D). The data in Fig. 2F represent the observation of a PDW state in a TMD material, $NbSe_2$.

In a PDW state, the energy gap $\Delta_P(\boldsymbol{r})$ should also modulate at $\boldsymbol{Q}_P$ (Eq. 3). We define the total gap $|\Delta(\boldsymbol{r})| = |\Delta_P(\boldsymbol{r}) + \Delta_S|$ to be half the energy separation between two coherence

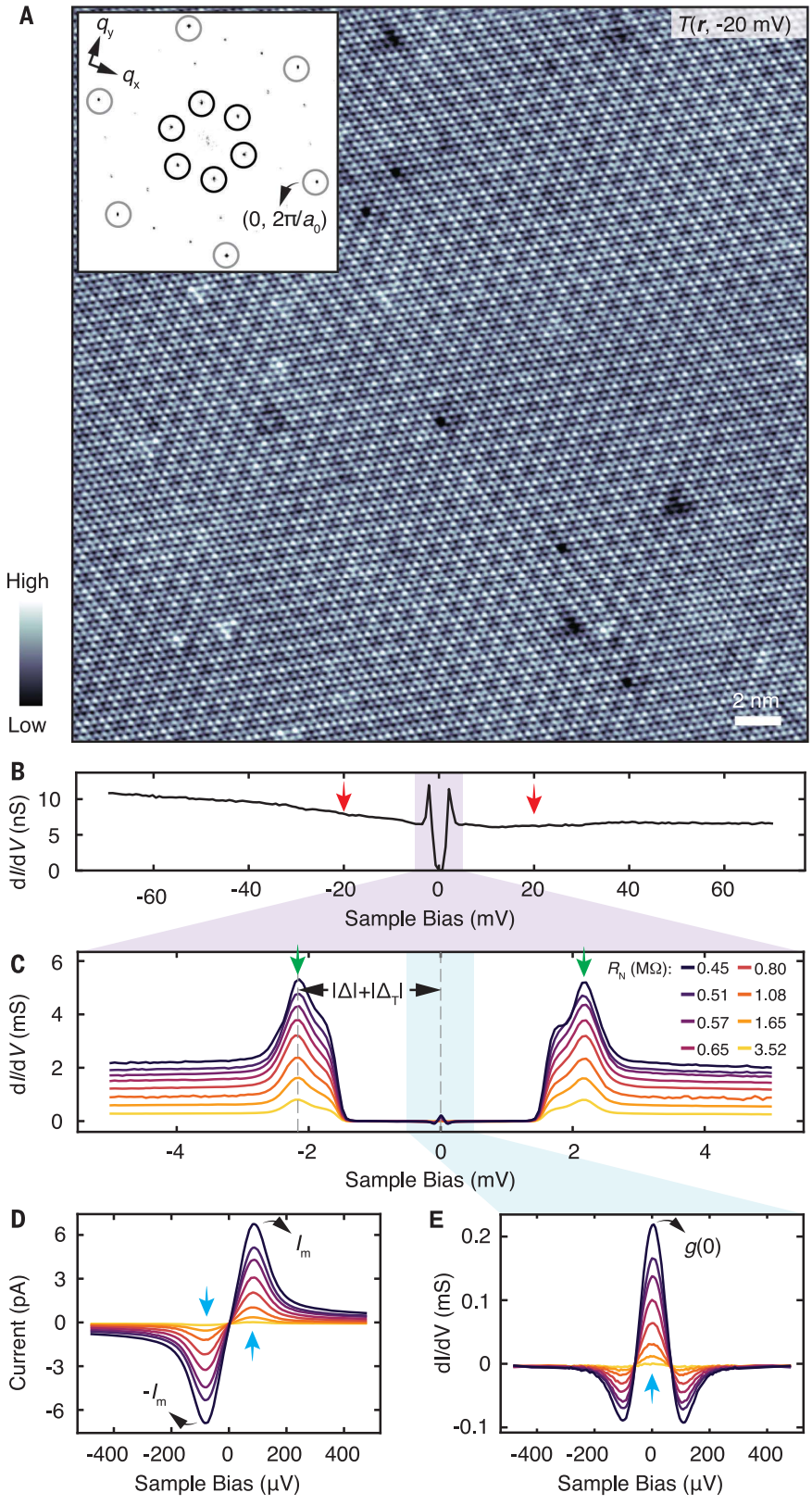

Fig. 1. Simultaneous single-electron and electron-pair tunneling spectroscopy. (**A**) Topographic image $T(\boldsymbol{r})$ of Se-termination surface of $NbSe_2$ measured at T = 290 mK. (Inset) The Fourier transform $T(\boldsymbol{q})$ with Bragg peaks $\boldsymbol{Q}_B^i \approx \{(1,0); (1/2, \sqrt{3}/2); (-1/2, \sqrt{3}/2)\}2\pi/a_0$ indicated with gray circles and the CDW peaks $\boldsymbol{Q}_C^i \approx \{(1,0); (1/2, \sqrt{3}/2); (-1/2, \sqrt{3}/2)\}2\pi/3a_0$ indicated with black circles. (**B**) Typical differential tunneling conductance spectrum $g(V) \equiv dI/dV(V)$ from a Nb scan-tip to $NbSe_2$ surface at T = 290 mK. The range of energies at which CDW modulations are intense in $g(V)$ is indicated approximately with red arrows. (**C**) Energy range in (B) is zoomed to show typical $g(V)$ characteristic owing to the combination of the superconducting energy gaps Δ_T of the Nb tip and Δ of the $NbSe_2$. The range of energies at which superconducting coherence peaks are intense in $g(V)$ is indicated with green arrows. (**D**) Measured electron-pair tunnel current $I_{CP}(V)$ in the phase-diffusive Josephson effect energy range $|E| \lesssim 100$ μeV, with the range of energies at which electron-pair current is maximum ($\pm I_m$) indicated with blue arrows. (**E**) Energy in (C) is zoomed to show phase-diffusive Josephson effect energy range, and the measured $g(V)$ whose $g(0) \propto I_J^2$ from Eq. 6 is indicated with a blue arrow.

peaks minus $|\Delta_T|$ (Fig. 1C). Our measured $|\Delta(\boldsymbol{r})|$ then exhibits modulations at three wave vectors $\boldsymbol{Q}_P^i \approx \{(1,0);(1/2,\sqrt{3}/2);(-1/2,\sqrt{3}/2)\}2\pi/3a_0$ (fig. S7) [(*23*), section 4]. This confirms independently, by use of single-electron tunneling, the existence of a PDW state in $NbSe_2$. Its gap modulation amplitude $|\Delta_P| < 0.01|\Delta_0|$ [(*23*), section 4]. A plot of the measured Fourier amplitudes of simultaneous $N_Q(|\boldsymbol{q}|)$ and $N_{CP}(|\boldsymbol{q}|)$ in the directions of $\boldsymbol{Q}_P^i \approx \boldsymbol{Q}_C^i$ is shown in Fig. 3A. The key maxima occur near $|q| = 2\pi/3a_0$, establishing quantitatively that $|\boldsymbol{Q}_P^i| = |\boldsymbol{Q}_C^i| \pm 1\%$. But, although imaged in precisely the same field of view (FOV), the charge density modulations (Fig. 2E) and electron-pair density modulations (Fig. 2F) appear distinctly different, with normalized cross correlation coefficient $\eta \approx -0.4$.

Possible microscopic mechanisms for a PDW state include Zeeman splitting (*30*, *31*) of a Fermi surface (not relevant here) and strongly correlated electron-electron interactions generating intertwined CDW and PDW states (*32*, *33*). But whatever the microscopic PDW mechanism for $NbSe_2$, Ginzburg-Landau (GL) theory allows a general analysis of interactions between SSC and CDW states. Consider a didactic GL free-energy density

$$\mathcal{F} = \mathcal{F}_S + \mathcal{F}_C + \mathcal{F}_P + \sum\nolimits_i \left(\lambda_i \rho_i \Delta_S^* \Delta_i + c.c.\right) \qquad (7)$$

Here, $\mathcal{F}_S$, $\mathcal{F}_C$, and $\mathcal{F}_P$ are the free energy densities of a SSC state (Eq. 2), a CDW state (Eq. 1), and a PDW state (Eq. 3), respectively. The term $\lambda_i \rho_i \Delta_S^* \Delta_i$ represents lowest-order coupling of the SSC and CDW states with a PDW and induces $\Delta_P^i(\boldsymbol{r})$ at wave vectors $\boldsymbol{Q}_P^i = Q_C^i$ owing to interactions of $\rho_C^i(\boldsymbol{r})$ and Δ_S. But the relative spatial arrangements of $\rho_C^i(\boldsymbol{r})$ and $\rho_P^i(\boldsymbol{r}) \propto \left|\Delta_P^i(\boldsymbol{r})\right|^2$ are ambiguous because if $\rho_C^i(\boldsymbol{r}) \propto \cos\left[\boldsymbol{Q}_C^i \cdot \boldsymbol{r} + \Phi_C^i(\boldsymbol{r})\right]$ and $\rho_P^i(\boldsymbol{r}) \propto \cos\left[\boldsymbol{Q}_P^i \cdot \boldsymbol{r} + \Phi_P^i(\boldsymbol{r})\right]$ and $\boldsymbol{Q}_P^i = \boldsymbol{Q}_C^i$, the phase difference $\delta\Phi^i(\boldsymbol{r}) \equiv \Phi_P^i(\boldsymbol{r}) - \Phi_C^i(\boldsymbol{r})$ cannot be predicted from Eq. 7.

To explore the GL predictions, we next visualized quasiparticle density $N_Q(\boldsymbol{r})$ and electron-pair density $N_{CP}(\boldsymbol{r})$ centered on a quantized vortex core (figs. S8 and S9) [(*23*), section 5]. $N_P(\boldsymbol{r})$ of the PDW is shown in Fig. 3B, and the total $N_{CP}(\boldsymbol{r})$ is shown in Fig. 3C. The background superfluid density $N_S(\boldsymbol{r}) = N_{CP}(\boldsymbol{r}) - N_P(\boldsymbol{r})$ is azimuthally symmetric about the core, which is consistent with previous experiments (*34*) and GL theory (*35*). The mutual decay of the PDW and SSC into the vortex along the yellow dashed lines in Fig. 3, B and C, is visualized in Fig. 3, D and E. More quantitatively, if $N_C^i(\boldsymbol{r}) = A_C^i(\boldsymbol{r}) \cos\left[\boldsymbol{Q}_C^i \cdot \boldsymbol{r} + \Phi_C^i(\boldsymbol{r})\right]$ and $N_P^i(\boldsymbol{r}) = A_P^i(\boldsymbol{r}) \cos\left[\boldsymbol{Q}_P^i \cdot \boldsymbol{r} + \Phi_P^i(\boldsymbol{r})\right]$, the combined PDW amplitude is represented by $A_P^{RMS}(\boldsymbol{r})\sqrt{\sum_{i=1}^{3}\left[A_P^i(\boldsymbol{r})\right]^2/3}$ in Fig. 3F [(*23*), section 6], demonstrating its mutual decay with $N_S(\boldsymbol{r})$ of SSC in Fig. 3G. This is as expected within GL theory (Eq. 7) for a CDW-induced PDW state.

Even though the PDW state is strongly linked to the parent SSC state (Fig. 3) and to the modulation wave vectors of the CDW state (Figs. 2D and 3A), the two modulating states appear spatially disparate at the atomic scale (Fig. 2, E and F). To explore this unexpected phenomenon, we visualized the amplitude and phase of the CDW and PDW for all three wave vectors $\boldsymbol{Q}_C^i \approx \boldsymbol{Q}_P^i$ (fig. S10). Shown in Fig. 4A is measured $A_C^1(\boldsymbol{r})$ from Fig. 2A, and shown in Fig. 4B is the simultaneously measured $A_P^1(\boldsymbol{r})$ from Fig. 2D. Both show nanoscale variations in the magnitude of their order parameters that are spatially alike, which is consistent with Eq. 7. Shown in Fig. 4, C and D, are the $\Phi_C^1(\boldsymbol{r})$ and $\Phi_P^1(\boldsymbol{r}) - 2\pi/3$ simultaneously obtained with

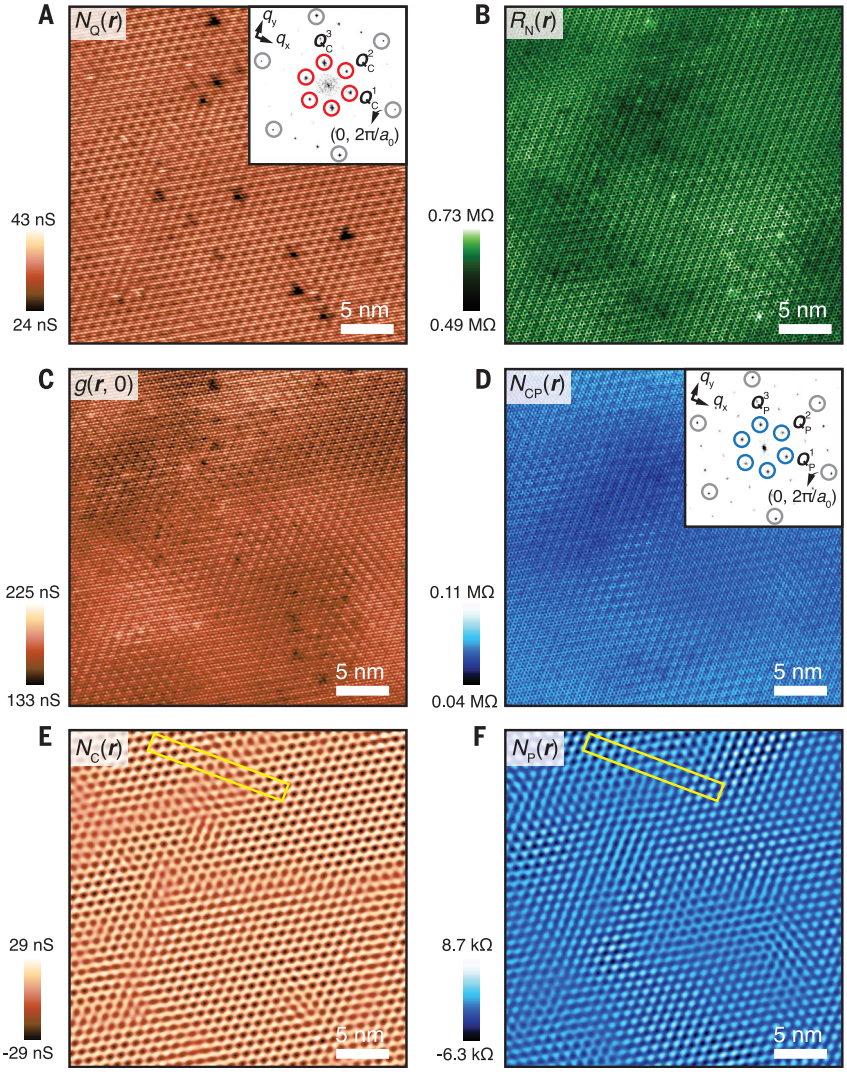

Fig. 2. Atomic-scale electron-pair tunneling visualization of a PDW state. (**A**) Measured $N_Q(\boldsymbol{r}) \equiv g(\boldsymbol{r}, -20\ mV)$ in the same FOV as Fig. 1A with pixel size ~30 pm at T = 290 mK. (Inset) $N_Q(\boldsymbol{q})$, with CDW peaks indicated with red circles. (**B**) Simultaneously measured $R_N(\boldsymbol{r}) = I^{-1}(\boldsymbol{r}, -4.5\ mV)$ as in (A). The purpose of this measurement is to establish the normal-state tip-sample junction resistance. (**C**) Simultaneously measured $g(r, 0) \propto I_J^2(\boldsymbol{r})$ as in (A). (**D**) Measured electron-pair density $N_{CP}(\boldsymbol{r}) \equiv g(\boldsymbol{r}, 0)R_N^2(\boldsymbol{r})$ from (B) and (C). (Inset) The PDW peaks in $N_{CP}(\boldsymbol{q})$ are indicated with blue circles. (**E**) Pure CDW charge density modulations $N_C(\boldsymbol{r})$ from (A). These are visualized at wave vectors $\boldsymbol{Q}_C^i \cong \{(1,0);(1/2,\sqrt{3}/2);(-1/2,\sqrt{3}/2)\}2\pi/3a_0$ by means of Fourier filtering $N_Q(\boldsymbol{r})$ at the CDW peaks indicated with red circles. (**F**) Pure electron-pair density modulations $N_P(\boldsymbol{r})$ from (D). These are visualized at wave vectors $\boldsymbol{Q}_P^i \cong \{(1,0);(1/2,\sqrt{3}/2);(-1/2,\sqrt{3}/2)\}2\pi/3a_0$ by means of Fourier filtering $N_{CP}(\boldsymbol{r})$ at the PDW peaks indicated with blue circles. There is a virtual absence of influence by impurity atoms or atomic-scale defects on the PDW state, as also seen in fig. S13.

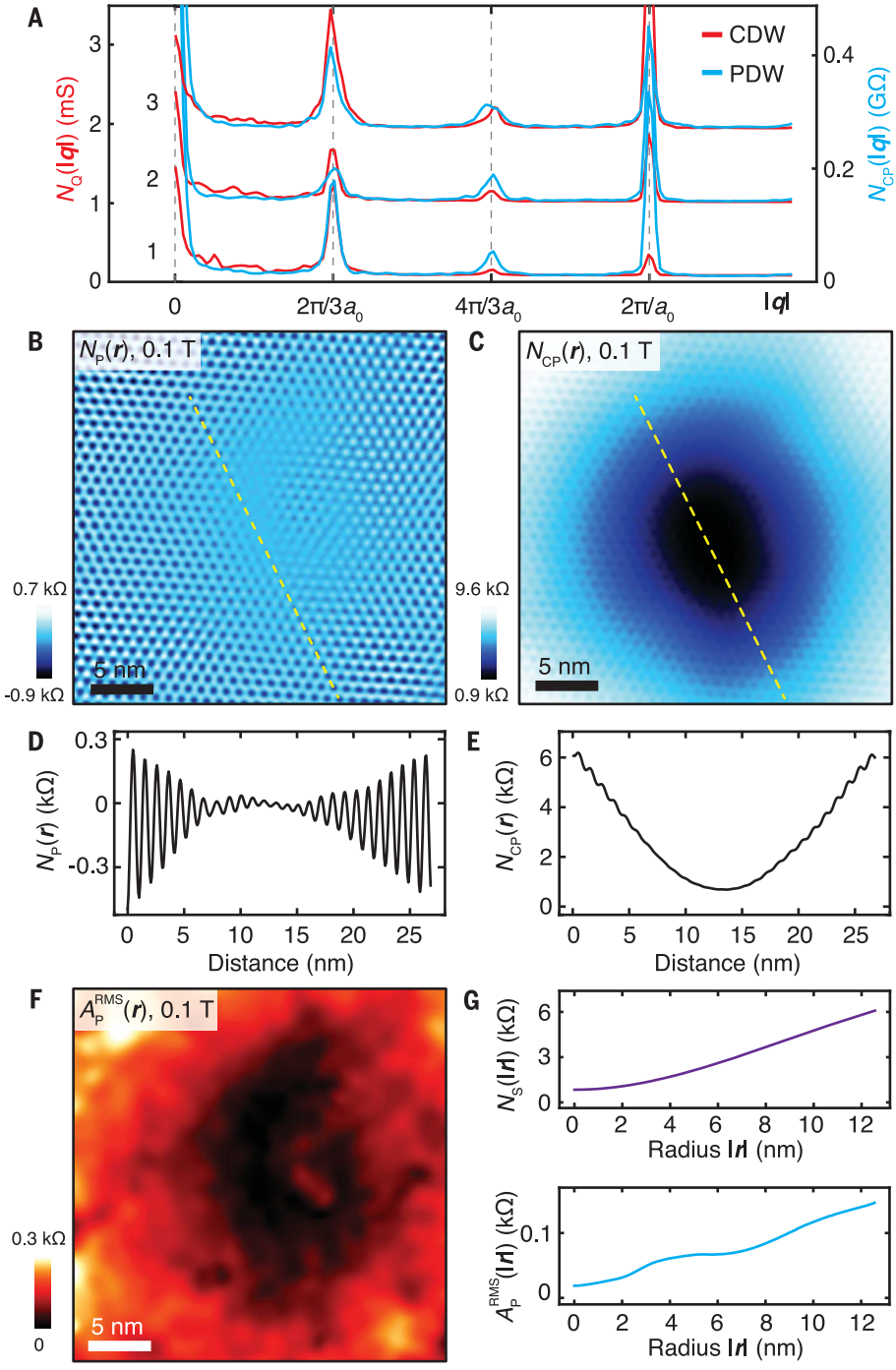

Fig. 3. Mutual decay of superconductivity and PDW into quantized vortex core. (**A**) Simultaneously measured amplitudes of charge density modulations $N_{\boldsymbol{Q}}(|\boldsymbol{q}|)$ (red) and electron-pair density modulations $N_{CP}(|\boldsymbol{q}|)$ (blue) at T = 290 mK, where $\boldsymbol{Q}_P^i \approx \boldsymbol{Q}_C^i$ is evident. (**B**) Measured PDW electron-pair density modulations at $\boldsymbol{Q}_P^i$, $N_P(\boldsymbol{r})$, centered on the core of a quantized vortex at B = 0.1 T and T = 290 mK. (**C**) Measured electron-pair density $N_{CP}(\boldsymbol{r})$ centered on vortex in (B). (**D**) Line profile of $N_P(\boldsymbol{r})$ along the yellow dashed line in (B). (**E**) Line profile of $N_{CP}(\boldsymbol{r})$ along the yellow dashed line in (C). (**F**) Measured PDW amplitude $A_P^{RMS}(\boldsymbol{r})$ centered on the vortex core. (**G**) The azimuthally averaged $N_S(|\boldsymbol{r}|)$ centered on the vortex core symmetry point, and similarly the azimuthally averaged RMS amplitude of all three PDW modulations $A_P^{RMS}(|\boldsymbol{r}|)$.

Fig. 4, A and B, which are very similar but only when a phase shift of $2\pi/3$ is subtracted everywhere from the measured $\Phi_P^1(\boldsymbol{r})$. In Fig. 4E, we show the histogram of $\delta\Phi^1(\boldsymbol{r}) = \Phi_P^1(\boldsymbol{r}) - \Phi_C^1(\boldsymbol{r})$ from Fig. 4, C and D, and in Fig. 4F, we show a combined histogram of all $|\delta\Phi^1(\boldsymbol{r})|$ $(i = 1, 2, 3)$. Hence, the relative spatial phase of the PDW and CDW states is globally $|\delta\Phi| \approx \pm 2\pi/3$. Experimentally measured $N_C^1(\boldsymbol{r})$ and $N_P^1(\boldsymbol{r})$ are shown in Fig. 4G merging with simultaneously measured topography $T(\boldsymbol{r})$ from the same FOV (Fig. 2, E and F, yellow boxes), revealing that an a_0 displacement between $N_C^1(\boldsymbol{r})$ and $N_P^1(\boldsymbol{r})$ generates this universal $\pm 2\pi/3$ phase shift.

So, what generates and controls this complex new PDW state at atomic scale? First, Bloch-state modulations at crystal-lattice periodicity will lead inevitably to lattice-periodic modulations of $N_Q(\boldsymbol{r})$, $N_{CP}(\boldsymbol{r})$, and $\Delta(\boldsymbol{r})$ [(*23*), section 7]. However, at a more sophisticated and specific level, a multiband plus anisotropic energy-gap theory of $NbSe_2$ has been developed to describe superconductive electronic structure modulations at the atomic scale (*36*). Beyond this, lattice strain is important in CDW physics of TMD materials (*13*, *16*). Lattice-locked 3×3 commensurate CDW domains occur in $NbSe_2$, separated by discommensurations at which the CDW phase jumps by $\delta\Phi_C = \pm 2\pi/3$ (*28*). We detected these $\delta\Phi_C = \pm 2\pi/3$ discommensurations, for example, in $\Phi_C^1(\boldsymbol{r})$ (Fig. 4C and fig. S11) and found $\delta\Phi_P = \pm 2\pi/3$ phase slips for the PDW state at virtually identical locations, along its domain boundaries in Fig. 4D. This might be expected if the PDW is induced by the CDW coupling to the superconductivity because the PDW domains would replicate those of the preexisting CDW. Moreover, the interstate phase-difference $|\delta\Phi| = |\Phi_P(\boldsymbol{r}) - \Phi_C(\boldsymbol{r})| \approx \pm 2\pi/3$ occurs universally (Fig. 4, C and D), not just at the commensurate domain boundaries. Hence, the simplest overall explanation is that the global phase shift $|\delta\Phi|$ does not originate from an independent lattice-lock-in of the PDW [(*23*), section 8].

As to atomic-scale interactions between the CDW and the SSC states, one must consider Cooper pairing in the presence of the CDW periodic potential $V(\boldsymbol{r})$. Solving the linearized superconducting gap equation does generate a nonzero $\Delta_P(\boldsymbol{r})$ with $\boldsymbol{Q}_P = \boldsymbol{Q}_C$ (*37*). More intuitively, electron pairing occurs not only at momenta $(\boldsymbol{k}, -\boldsymbol{k})$ but also $(\boldsymbol{k} + \boldsymbol{G}, -\boldsymbol{k})$ and $(\boldsymbol{k}, -\boldsymbol{k} + \boldsymbol{G})$, where $\boldsymbol{G}$ is a reciprocal-lattice vector of the CDW state: $\boldsymbol{G} = m\boldsymbol{Q}_C$; m = 0, ±1, ±2, ... (fig. S12). The consequent electron-pair density at lowest order in $\boldsymbol{G}$ [(*23*), section 9] is

$$\rho_P(\boldsymbol{r}) \propto \cos\left(\boldsymbol{Q}_C \cdot \boldsymbol{r} + \Phi_C^{\boldsymbol{Q}_C} + \delta\Phi\right) \qquad (8)$$

Thus, the electron-pair density modulates spatially at the wave vectors $\pm\boldsymbol{Q}_C$ owing to the finite center-of-mass electron-pair momentum $(\pm\hbar\boldsymbol{Q}_C)$ imposed by the CDW. Moreover, this same approach shows that a phase difference $|\delta\Phi| = \left|\Phi_P^{\boldsymbol{Q}_C} - \Phi_C^{\boldsymbol{Q}_C}\right|$ is determined by the $\boldsymbol{k}$-space structure factor of the electron-pair wave function [(*23*), section 9]. Last, at the single-atom scale, we found that impurity atoms leave the PDW state virtually unperturbed

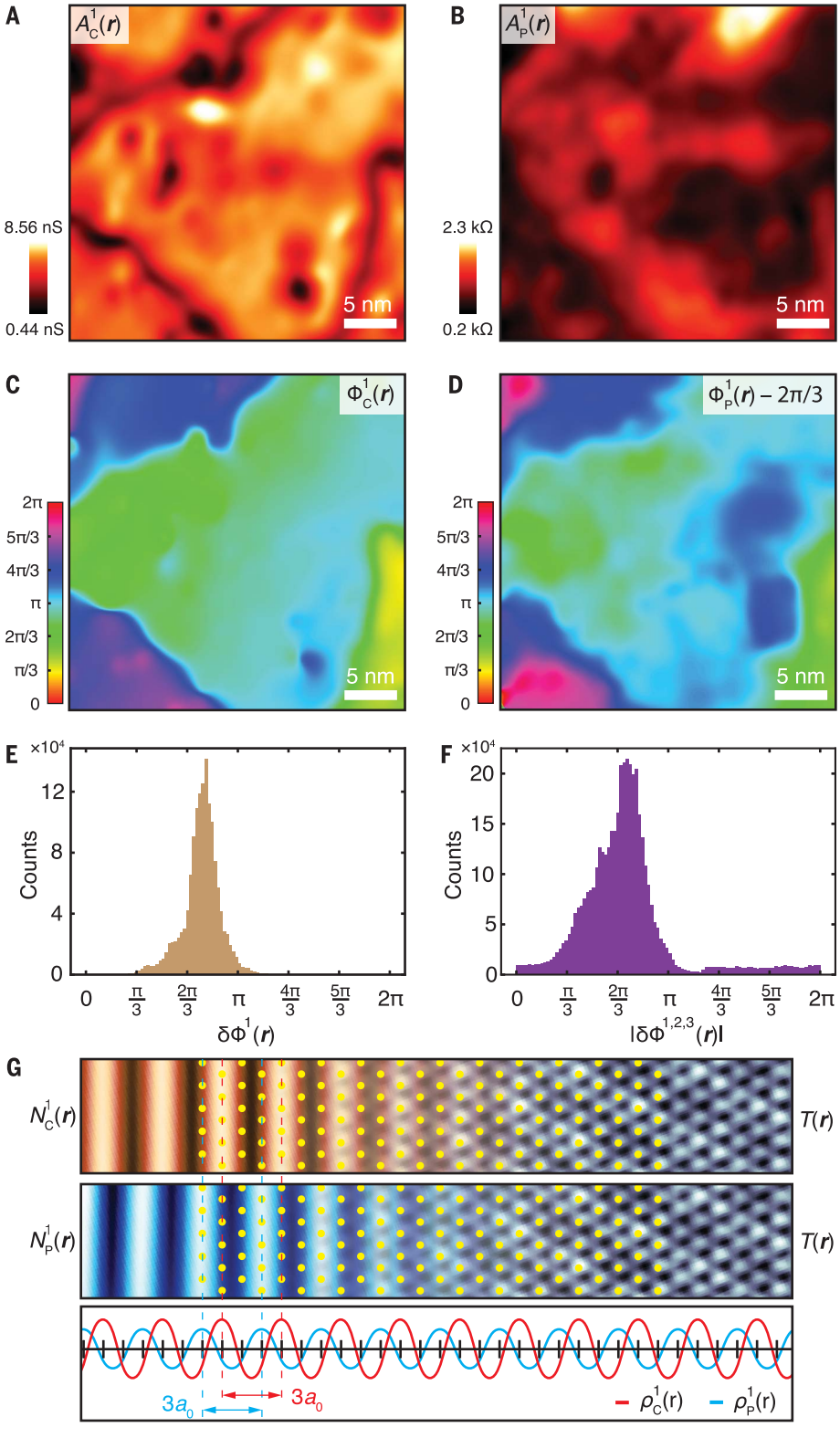

Fig. 4. Inter-state discommensuration of the CDW and PDW states. (**A**) Measured CDW amplitude of $A_C^1(\boldsymbol{r})$ for modulations at $\boldsymbol{Q}_C^1$ from Fig. 2A. All data shown in (A) to (D) were measured in the FOV of Fig. 1A, with the resulting electronic structure images shown in Fig. 2. (**B**) Simultaneously measured PDW amplitude of $A_P^1(\boldsymbol{r})$ for modulations at $\boldsymbol{Q}_P^1$ from Fig. 2D. (**C**) Measured CDW spatial phase $\Phi_C^1(\boldsymbol{r})$ for modulations at $\boldsymbol{Q}_C^1$ [simultaneous with (A)]. Our measurements found that $\Phi_C^1(\boldsymbol{r})$ is virtually independent of the bias voltage V for $-70\ \text{mV} \leq V \leq -10\ \text{mV}$ (fig. S14) and impervious to atomic defects (fig. S15). (**D**) Measured PDW spatial phase $\Phi_P^1(\boldsymbol{r}) - \frac{2\pi}{3}$ for modulations at $\boldsymbol{Q}_P^1$ [simultaneous with (B)]. (**E**) Histogram of $\delta\Phi^1(\boldsymbol{r}) \equiv \Phi_P^1(\boldsymbol{r}) - \Phi_C^1(\boldsymbol{r})$ from (C) and (D). (**F**) Histograms of $|\delta\Phi^i(\boldsymbol{r})| \equiv |\Phi_P^i(\boldsymbol{r}) - \Phi_C^i(\boldsymbol{r})|$ for i = 1, 2, 3 from Fig. 2, A,and D. This result is also independently supported by the cross-correlation coefficient ($\eta_E = -0.44$) between $N_C(\boldsymbol{r})$ and $N_P(\boldsymbol{r})$ (Fig. 2, E and F) closely matching that of simulated images ($\eta_S = -0.5$) with $2\pi/3$ inter-state phase difference (fig. S16). (**G**) (Top and middle) Experimentally measured $N_C^1(\boldsymbol{r})$ and $N_P^1(\boldsymbol{r})$ merging with simultaneously measured topography $T(\boldsymbol{r})$ from the same FOV (Fig. 2, E and F, yellow boxes) with Se atoms indicated by yellow dots. (Bottom) Schematic of the PDW:CDW inter-state discommensurations with $\delta\Phi^1(\boldsymbol{r}) = \frac{2\pi}{3}$.

(fig. S13), implying that Anderson's theorem also pertains to an *s*-wave PDW.

The techniques and observations reported here herald abundant and exciting PDW physics in the many TMDs that, like $NbSe_2$, sustain both CDW and superconducting states.

REFERENCES AND NOTES

1. S. Manzeli, D. Ovchinnikov, D. Pasquier, O. V. Yazyev, A. Kis, *Nat. Rev. Mater.* **2**, 17033 (2017).
2. A. Kogar *et al.*, *Science* **358**, 1314–1317 (2017).
3. P. Li *et al.*, *Nat. Commun.* **8**, 2150 (2017).
4. J. Gooth *et al.*, *Nat. Commun.* **9**, 4093 (2018).
5. S. Ran *et al.*, *Science* **365**, 684–687 (2019).
6. L. Jiao *et al.*, *Nature* **579**, 523–527 (2020).
7. D. F. Agterberg *et al.*, *Annu. Rev. Condens. Matter Phys.* **11**, 231–270 (2020).
8. D. Möckli, Y. Yanase, M. Sigrist, *Phys. Rev. B* **97**, 144508 (2018).
9. J. Venderley, E.-A. Kim, *Sci. Adv.* **5**, eaat4698 (2019).
10. C. Chen, L. Su, A. H. Castro Neto, V. M. Pereira, *Phys. Rev. B* **99**, 121108 (2019).
11. K. Slagle, L. Fu, *Phys. Rev. B* **102**, 235423 (2020).

12. D. F. Agterberg, M. Geracie, H. Tsunetsugu, . *Phys. Rev. B Condens. Matter Mater. Phys.* **84**, 014513 (2011).
13. A. Soumyanarayanan *et al*., *Proc. Natl. Acad. Sci. U.S.A.* **110**, 1623–1627 (2013).
14. J. Okamoto, C. J. Arguello, E. P. Rosenthal, A. N. Pasupathy, A. J. Millis, *Phys. Rev. Lett.* **114**, 026802 (2015).
15. H. M. Hill, A. F. Rigosi, K. T. Rim, G. W. Flynn, T. F. Heinz, *Nano Lett.* **16**, 4831–4837 (2016).
16. S. Gao *et al*., *Proc. Natl. Acad. Sci. U.S.A.* **115**, 6986–6990 (2018).
17. S. H. Pan, E. W. Hudson, J. C. Davis, *Appl. Phys. Lett.* **73**, 2992–2994 (1998).
18. J. Šmakov, I. Martin, A. V. Balatsky, *Phys. Rev. B Condens. Matter Mater. Phys.* **64**, 212506 (2001).
19. M. Graham, D. K. Morr, *Phys. Rev. Lett.* **123**, 017001 (2019).
20. O. Naaman, W. Teizer, R. C. Dynes, *Phys. Rev. Lett.* **87**, 097004 (2001).
21. Y. M. I. Anchenko, *Sov. Phys. JETP* **55**, 2395–2402 (1969).
22. G.-L. Ingold, H. Grabert, U. Eberhardt, *Phys. Rev. B Condens. Matter* **50**, 395–402 (1994).
23. Materials and methods and supplementary text are available as supplementary materials.
24. H. Kimura, R. P. Barber Jr., S. Ono, Y. Ando, R. C. Dynes, *Phys. Rev. Lett.* **101**, 037002 (2008).
25. V. Crespo *et al*., *Physica C* **479**, 19–23 (2012).
26. M. H. Hamidian *et al*., *Nature* **532**, 343–347 (2016).
27. M. T. Randeria, B. E. Feldman, I. K. Drozdov, A. Yazdani, *Phys. Rev. B* **93**, 161115 (2016).
28. D. Cho, K. M. Bastiaans, D. Chatzopoulos, G. D. Gu, M. P. Allan, *Nature* **571**, 541–545 (2019).
29. W. L. McMillan, *Phys. Rev. B Condens. Matter* **14**, 1496–1502 (1976).
30. P. Fulde, R. A. Ferrell, *Phys. Rev.* **135** (3A), A550–A563 (1964).
31. A. I. Larkin, Y. N. Ovchinnikov, *Sov. Phys. JETP* **20**, 762–762 (1965).
32. E. Fradkin, S. A. Kivelson, J. M. Tranquada, *Rev. Mod. Phys.* **87**, 457–482 (2015).
33. P. Choubey *et al*., *Proc. Natl. Acad. Sci. U.S.A.* **117**, 14805–14811 (2020).
34. H. Suderow, I. Guillamón, J. G. Rodrigo, S. Vieira, *Supercond. Sci. Technol.* **27**, 063001 (2014).
35. A. A. Abrikosov, *J. Exp. Theor. Phys.* **32**, 1147–1182 (1957).
36. I. Guillamon, H. Suderow, F. Guinea, S. Vieira, *Phys. Rev. B Condens. Matter Mater. Phys.* **77**, 134505 (2008).
37. K. Machida, T. Koyama, T. Matsubara, *Phys. Rev. B Condens. Matter* **23**, 99–105 (1981).
38. X. Liu, Y. X. Chong, R. Sharma, J. C. S. Davis, Data associated with "Discovery of a Cooper-pair density wave state in a transition-metal dichalcogenide". Zenodo (2021).

ACKNOWLEDGMENTS

The authors acknowledge and thank D.-H. Lee and E. Fradkin for key theoretical guidance and M. P. Allan, K. M. Bastiaans, K. Fujita, and S. A. Kivelson for helpful discussions and advice. **Funding:** X.L. acknowledges support from Kavli Institute at Cornell. Y.X.C., R.S., and J.C.S.D. acknowledge support from the Moore Foundation's EPiQS Initiative through grant GBMF9457. J.C.S.D. acknowledges support from Science Foundation Ireland under award SFI 17/RP/5445 and from the European Research Council (ERC) under award DLV-788932. **Author contributions:** X.L, Y.X.C., and J.C.S.D. developed and carried out the experiments; X.L., Y.X.C., and R.S. developed and implemented analysis. J.C.S.D. supervised the project. The paper reflects contributions and ideas of all authors. **Competing interests:** The authors declare no competing interests. **Data and materials availability:** All data are available in the main text, in the supplementary materials, and on Zenodo (*38*).

SUPPLEMENTARY MATERIALS

science.sciencemag.org/content/372/6549/1447/suppl/DC1
Materials and Methods
Supplementary Text
Figs. S1 to S16
References (*39*–*55*)

22 June 2020; accepted 18 May 2021
10.1126/science.abd4607

Discovery of a Cooper-pair density wave state in a transition-metal dichalcogenide

Xiaolong Liu, Yi Xue Chong, Rahul Sharma and J. C. Séamus Davis

Science **372** (6549), 1447-1452.
DOI: 10.1126/science.abd4607

Imaging an exotic state

Among the most intriguing of the many phases of cuprate superconductors is the so-called pair density wave (PDW) state. PDW is characterized by a spatially modulated density of Cooper pairs and can be detected with a scanning tunneling microscope equipped with a superconducting tip. Liu *et al.* used Josephson tunneling microscopy, modified for the task, to detect PDW in niobium diselenide, a superconductor with a layered hexagonal structure. The PDW state is expected to appear in other transition metal dichalcogenides as well.

Science, abd4607, this issue p. 1447